

Electromagnetic wave absorption properties of $Ba(CoTi)_xFe_{12-2x}O_{19}$@$BiFeO_3$ in hundreds of megahertz band

Zhi-Biao Xu(徐志彪), Zhao-Hui Qi(齐照辉), Guo-Wu Wang(王国武), Chang Liu(刘畅), Jing-Hao Cui(崔晶浩), Wen-Liang Li(李文梁), and Tao Wang(王涛)

Citation: Chin. Phys. B, 2022, 31 (**8**): 087504. DOI: 10.1088/1674-1056/ac5240
Journal homepage: http://cpb.iphy.ac.cn; http://iopscience.iop.org/cpb

What follows is a list of articles you may be interested in

Enhancement of magnetic and dielectric properties of low temperature sintered NiCuZn ferrite by Bi_2O_3-CuO additives

Jie Li(李颉), Bing Lu(卢冰), Ying Zhang(张颖), Jian Wu(武剑), Yan Yang(杨燕), Xue-Ning Han(韩雪宁), Dan-Dan Wen(文丹丹), Zheng Liang(梁峥), and Huai-Wu Zhang(张怀武)

Chin. Phys. B, 2022, 31 (**4**): 047502. DOI: 10.1088/1674-1056/ac3399

Incommensurate-commensurate magnetic phase transition in double tungstate $Li_2Co(WO_4)_2$

Xiyu Chen(陈西煜), Ning Ding(丁宁), Meifeng Liu(刘美风), Tao Zou(邹涛), V. Ovidiu Garlea, Jingwen Gong(龚婧雯), Fei Liu(刘飞), Yunlong Xie(谢云龙), Lun Yang(杨伦), Shuhan Zheng(郑书翰), Xiuzhang Wang(王秀章), Shuai Dong(董帅), T. Charlton, and Jun-Ming Liu(刘俊明)

Chin. Phys. B, 2022, 31 (**4**): 047501. DOI: 10.1088/1674-1056/ac3818

Magnetocrystalline anisotropy and dynamic spin reorientation of half-doped $Nd_{0.5}Pr_{0.5}FeO_3$ single crystal

Haotian Zhai(翟浩天), Tian Gao(高湉), Xu Zheng(郑旭), Jiali Li(李佳丽), Bin Chen(陈斌), Hongliang Dong(董洪亮), Zhiqiang Chen(陈志强), Gang Zhao(赵钢), Shixun Cao(曹世勋), Chuanbing Cai(蔡传兵), and Vyacheslav V. Marchenkov

Chin. Phys. B, 2021, 30 (**7**): 077502. DOI: 10.1088/1674-1056/ac0786

High permeability and bimodal resonance structure of flaky soft magnetic composite materials

Xi Liu(刘曦), Peng Wu(吴鹏), Peng Wang(王鹏), Tao Wang(王涛), Liang Qiao(乔亮), Fa-Shen Li(李发伸)

Chin. Phys. B, 2020, 29 (**7**): 077506. DOI: 10.1088/1674-1056/ab8c3b

Multiferroic and enhanced microwave absorption induced by complex oxide interfaces

Cuimei Cao(曹翠梅), Chunhui Dong(董春晖), Jinli Yao(幺金丽), Changjun Jiang(蒋长军)

Chin. Phys. B, 2018, 27 (**1**): 017503. DOI: 10.1088/1674-1056/27/1/017503

Electromagnetic wave absorption properties of $Ba(CoTi)_xFe_{12-2x}O_{19}$@$BiFeO_3$ in hundreds of megahertz band

Zhi-Biao Xu(徐志彪)[1], Zhao-Hui Qi(齐照辉)[2], Guo-Wu Wang(王国武)[1], Chang Liu(刘畅)[1], Jing-Hao Cui(崔晶浩)[1], Wen-Liang Li(李文梁)[1], and Tao Wang(王涛)[1,†]

[1] *Key Laboratory of Magnetism and Magnetic Materials of the Ministry of Education, Lanzhou University, Lanzhou* 730000, *China*
[2] *The Institute of Effectiveness Evaluation of Flying Vehicle, Beijing* 100089, *China*

(Received 23 November 2021; revised manuscript received 22 January 2022; accepted manuscript online 7 February 2022)

The high-performance electromagnetic (EM) wave absorption material $Ba(CoTi)_xFe_{12-2x}O_{19}$@$BiFeO_3$ was prepared by solid-state reaction, and its EM wave absorption properties were deeply studied. The results revealed that $Ba(CoTi)_xFe_{12-2x}O_{19}$@$BiFeO_3$ could obtain excellent absorption properties in hundreds of megahertz by adjusting the Co^{2+}–Ti^{4+} content. The best comprehensive property was obtained for $x = 1.2$, where the optimal reflection loss (*RL*) value reaches −30.42 dB at about 600 MHz with thickness of 3.5 mm, and the corresponding effective absorption band covers the frequency range of 437 MHz–1 GHz. Moreover, the EM wave absorption mechanism was studied based on the simulation methods. The simulated results showed that the excellent EM wave absorption properties of $Ba(CoTi)_xFe_{12-2x}O_{19}$@$BiFeO_3$ mainly originated from the internal loss caused by natural resonance, and the interface cancelation further improved the absorption properties and resulted in *RL* peaks.

Keywords: microwave absorption, M-type ferrite, high permeability, impedance matching

PACS: 75.47.Lx, 78.20.Ci **DOI:** 10.1088/1674-1056/ac5240

1. Introduction

Nowadays, the rapid development of microwave technology and the widespread popularity of electronic communication equipment have brought convenience to human life.[1] The leakage from EM waves has also introduced excessive pollution to the environment, which threatens the physical and mental health of human.[2] Various EM wave absorption materials with excellent properties have been developed to eliminate the adverse effects of excessive EM radiation on human life.[3–6] These materials include dielectric materials[7–11] such as carbon materials,[12,13] nonmagnetic sulfides,[14] conjugated polymers[15] and magnetic materials such as ferrites,[16–19] magnetic metals,[20–22] and rare earth alloys.[23,24] However, most studies have mainly focused on EM wave absorption materials in the gigahertz range, whereas studies on absorption materials working in the hundreds of megahertz range are relatively rare.[25–27] This means that serious problems of EM pollution in the hundreds of megahertz band have not been well solved.[28] In this frequency range, effective absorption is difficult due to the long wavelength and insufficient dielectric or magnetic loss.[29–31] It is a serious challenge for researchers to explore materials with excellent absorption properties in the hundreds of megahertz bands.

Ferrite materials have attracted much attention of researchers as good EM wave absorption materials.[32] Among them, M-type barium ferrites ($BaFe_{12}O_{19}$) have been deeply investigated as an absorption material working in the gigahertz range because they have suitable permittivity, high stability, low density, and low cost.[33] However, the high resonance frequency and low permeability of M-type ferrites are not conducive to their absorption properties in the hundreds of megahertz band.[34] Related reports have indicated that co–substitution of trivalent iron ions in M-type ferrites by divalent (Co^{2+}, Mn^{2+}, Zn^{2+}, Ni^{2+}) and tetravalent (Ti^{4+}, Sn^{4+}, Zr^{4+}, Ir^{4+}) cations is a proven method for increasing the permeability and decreasing the resonance frequency.[35] Among these, Co^{2+}–Ti^{4+} co-substitution is considered as the most effective method for adjusting the absorption properties because that the substitution of Co^{2+} and Ti^{4+} for Fe^{3+} in barium ferrite can not only dramatically increase the permeability but also increase the magnetic loss in range of hundreds of megahertz.[36]

In this work, $Ba(CoTi)_xFe_{12-2x}O_{19}$ with high permeability in hundreds of megahertz was obtained by substituting Fe^{3+} distributed in five different lattice sites in $BaFe_{12}O_{19}$ with Co^{2+} and Ti^{4+}. The permittivity was optimized by the $BiFeO_3$ dielectric phase formed by doping with Bi_2O_3, thus obtaining superb impedance matching. The EM wave absorption properties for $Ba(CoTi)_xFe_{12-2x}O_{19}$@$BiFeO_3$ were studied in detail and its EM wave absorption mechanism was deeply discussed in hundreds of megahertz range.

2. Experiment

2.1. Fabrication

The target $Ba(CoTi)_xFe_{12-2x}O_{19}$ ferrite ceramics with $x = 0.9$, 1.0, 1.1, 1.2, 1.3, and 1.4 were prepared by the conventional solid-state reaction method. Analytical grade

†Corresponding author. E-mail: wtao@lzu.edu.cn

© 2022 Chinese Physical Society and IOP Publishing Ltd

$BaCO_3$ (AR grade, $\geq 99\%$), Co_2O_3 (AR grade, $\geq 99\%$), TiO_2 (AR grade, $\geq 99\%$), and Fe_2O_3 (AR grade, $\geq 99\%$), were mixed and ball milled in a planetary ball mill for 12 h. Then, the powders after ball milled were desiccated and pre-sintered at 1100 °C for 6 h in a tube furnace under the air atmosphere. The pre-sintered powders were secondly ball milled for 12 h with 5 wt% Bi_2O_3 in the same mill grinder. After drying, the powders were granulated by using 10.0 wt% polyvinyl alcohol (PVA) adhesive. Finally, the granulated particles were pressed at 1000 MPa for 10 min to form ring samples with an inner diameter of 3.04 mm, an outer diameter of 7 mm, and a thickness of 2–3 mm. The ring samples were sintered in the same furnace at 935 °C for 6 h to form bulk samples.

2.2. Characterization

The crystal structure of the bulk samples was characterized by x-ray diffraction (XRD) with a Cu-$K\alpha$ radiation source. The surface morphologies of bulk samples were characterized by using a scanning electron microscopy (SEM). The hysteresis loops of the bulk samples at room temperature were measured by using a vibrating sample magnetometer (VSM) to characterize the static magnetic properties of the material. The EM parameters of the bulk samples were measured at room temperature in a frequency range from 1 MHz to 1 GHz by using an impedance analyzer.

3. Results and discussion

3.1. Structural characterization

The XRD patterns of $Ba(CoTi)_xFe_{12-2x}O_{19}$ bulk samples with various x ($x = 0.9$, 1.1, 1.2, 1.3, and 1.4) are shown in Fig. 1(a). The results indicate that the crystal structure does not change significantly with the variation of Co^{2+}–Ti^{4+} content. The standard PDF cards and the crystal face index of the diffraction peaks are shown in Fig. 1(b). It can be clearly seen that the XRD patterns of bulk samples with various Co^{2+}–Ti^{4+} content show diffraction peaks that belong to two different phases. Some strong diffraction peaks are the M-type barium ferrite $Ba(CoTi)_xFe_{12-2x}O_{19}$ with hexagonal ferrite structure (PDF#39-1433), and the other diffraction peaks marked with red symbols are the $BiFeO_3$ with a typical rhombohedral perovskite structure (PDF#20-0169). Except for the two phases, no other impurity phases are detected in the XRD patterns of all bulk samples. This indicates that the addition of Bi_2O_3 does not affect the formation of $Ba(CoTi)_xFe_{12-2x}O_{19}$ phase,[37] and the Bi_2O_3 just combines with Fe^{3+} to form Bi–Fe compound ($BiFeO_3$).[38] Then, the $BiFeO_3$ enters into the interstice between the $Ba(CoTi)_xFe_{12-2x}O_{19}$ particles.[39]

The lattice parameters of the bulk samples change with the substitution of Fe^{3+} by Co^{2+}–Ti^{4+}. Among them, lattice constants a and c of the bulk samples are calculated using different diffraction peaks in the XRD patterns. The formula is as follows:

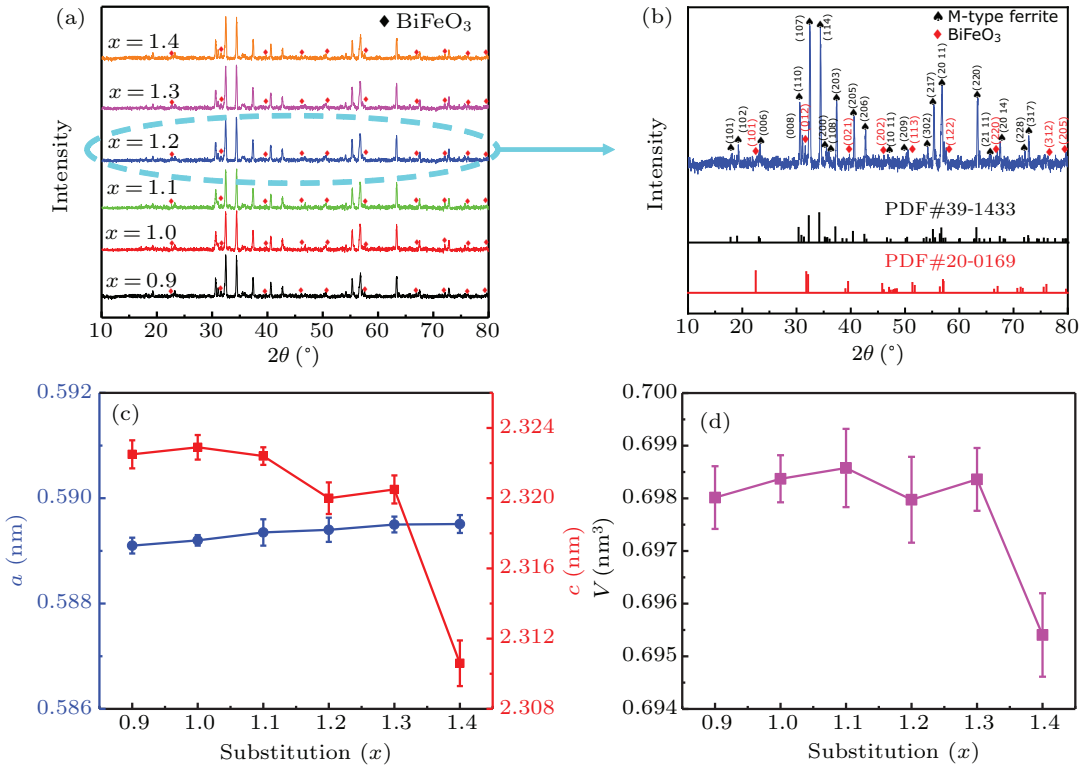


Fig. 1. (a) XRD patterns of the bulk samples with various x ($x = 0.9$, 1.0, 1.1, 1.2, 1.3, 1.4). (b) The standard cards and the crystal face index of the diffraction peaks. (c) Lattice constants a and c for the bulk samples with various x. (d) Cell volume V for the bulk samples.

$$d = \left[\frac{4}{3}\left(\frac{h^2+hk+k^2}{a^2}\right)+\frac{l^2}{c^2}\right]^{-1/2}. \quad (1)$$

Figure 1(c) shows the variation of lattice constants a and c as a function of Co–Ti content x. It can be seen that there is a slight and steady increase of the lattice constant a with Co–Ti substitution from 0.5891 nm to 0.5895 nm. The lattice constants c has an overall decreasing trend with increasing x. The cell volume V also has an overall decreasing trend, as x is changed from 0.9 to 1.4, and the result is in good agreement with researches conducted by Li *et al*.[45]

3.2. Morphological properties

Figures 2(a)–2(f) show the cross-sectional SEM images of bulk samples with various Co^{2+}–Ti^{4+} content. The SEM images show that the particle size of $Ba(CoTi)_xFe_{12-2x}O_{19}$@$BiFeO_3$ does not change significantly with the increase of Co^{2+}–Ti^{4+} content. The particle size is approximately 500 nm–2 μm in all bulk samples. The small particle size can be attributed to the liquid phase effect induced by the addition of excess Bi_2O_3 during the sintering process.[40,41] Figure 2(g) shows the local magnified view of the cross section for the bulk sample, where the part marked by the yellow dotted line is $Ba(CoTi)_xFe_{12-2x}O_{19}$ particles and the part marked by the blue dotted is $BiFeO_3$. It can be seen that the $Ba(CoTi)_xFe_{12-2x}O_{19}$ particles are coated by the $BiFeO_3$ formed during the sintering process. Figures 2(h)–2(i) show the elemental mapping images of $Ba(CoTi)_xFe_{12-2x}O_{19}$@$BiFeO_3$ bulk samples. The elements Ba, Fe, Co, and Ti are distributed uniformly inside the bulk samples. The element Bi is observed mainly at the surface of $Ba(CoTi)_xFe_{12-2x}O_{19}$ particles. It is further proved that $BiFeO_3$ is coated on the surface of $Ba(CoTi)_xFe_{12-2x}O_{19}$ particles.

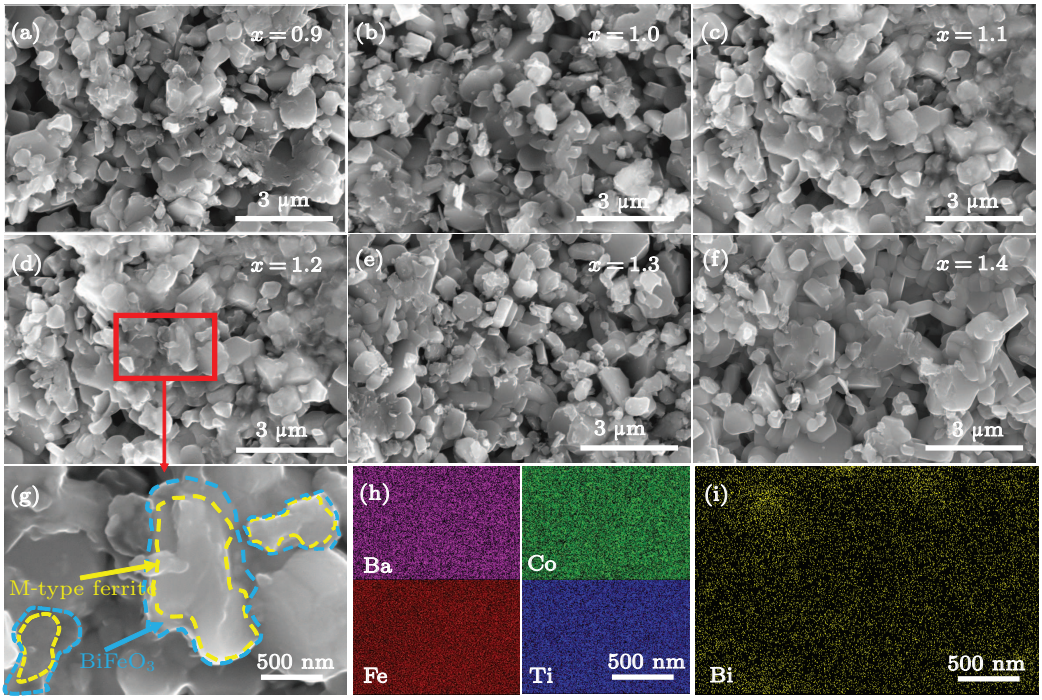


Fig. 2. (a)–(f) The SEM images of $Ba(CoTi)_xFe_{12-2x}O_{19}$@$BiFeO_3$: (a) $x = 0.9$, (b) $x = 1.0$, (c) $x = 1.1$, (d) $x = 1.2$, (e) $x = 1.3$, and (f) $x = 1.4$. (g) The local magnified view of the cross section for the bulk sample. (h)–(i) The elemental mapping images of $Ba(CoTi)_xFe_{12-2x}O_{19}$@$BiFeO_3$.

3.3. Static magnetic properties

The hysteresis loops of the $Ba(CoTi)_xFe_{12-2x}O_{19}$@$BiFeO_3$ bulk samples with various x are shown in Fig. 3(a). The results show that bulk samples exhibit typical soft-magnetic properties with the variation of x values. The variation of saturation magnetization (M_s) and coercivity (H_c) with different x are shown in Fig. 3(b). M_s decreases slightly with the increase of x. H_c decreases rapidly with increasing x from 0.9 to 1.1. As x continues to increase, H_c also decreases slowly. The static magnetic properties of $Ba(CoTi)_xFe_{12-2x}O_{19}$@$BiFeO_3$ mainly depend on the magnetic phase $Ba(CoTi)_xFe_{12-2x}O_{19}$. In the basic structure of $Ba(CoTi)_xFe_{12-2x}O_{19}$, Co^{2+} ions first preferentially occupy the $2a$ and $2b$ lattice sites and Ti^{4+} ions occupy $2a$ and $4f_2$ lattice sites.[42] The ions at the $2a$ and $2b$ lattice sites have an upward spin direction, while the ions at the $4f_2$ lattice sites have a downward spin direction.[43] M_s is determined by the magnetic moment of each metal cation and the amount of magnetic ions in each lattice site.[44] Therefore, as x increases from 0.9 to 1.4, M_s of the $Ba(CoTi)_xFe_{12-2x}O_{19}$@$BiFeO_3$ bulk sample decreases slightly. In addition, based on the S–W theory, $H_c \approx 2K_1/\mu_0 M_s$.[45] When the value of x is low, Co^{2+}–Ti^{4+} ions first preferentially occupy the $2a$, $2b$, and $4f_2$. This causes the magnetocrystalline anisotropy constant (K_1) value to decrease rapidly, then H_c decreases rapidly. As x continues to increase, more Co^{2+}–Ti^{4+} ions occupy the $2a$ and $4f_1$ sites, which leads to a slight decrease in K_1 value and a corresponding slow decrease in H_c.

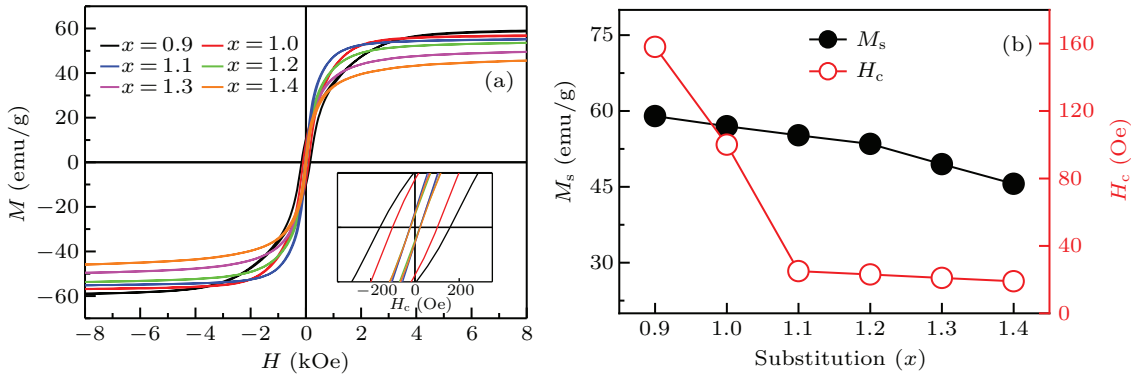


Fig. 3. (a) Magnetic hysteresis loops of $Ba(CoTi)_xFe_{12-2x}O_{19}$@$BiFeO_3$ with various x values. (b) Effects of Co^{2+}–Ti^{4+} content on M_s and H_c of $Ba(CoTi)_xFe_{12-2x}O_{19}$@$BiFeO_3$.

3.4. Complex permittivity and permeability

The dependence of complex permittivity and permeability on frequency of $Ba(CoTi)_xFe_{12-2x}O_{19}$@$BiFeO_3$ with various x are shown in Fig. 4. The real parts (ε') of the permittivity of all samples at 1 MHz–1 GHz are about 20, while the imaginary parts (ε'') are almost 0. For the samples with $x = 0.9$, 1.0, 1.1, 1.2, 1.3, and 1.4, the real parts (μ') of the permeability at 1 MHz can reach 2.51, 3.53, 15.46, 20.86, 16.38, and 13.49, while the imaginary parts (μ'') exhibit obvious peak between 100 MHz and 1 GHz for the samples with $x = 1.1$, 1.2, and 1.3. The above measurement results show that the substitution of Co^{2+}–Ti^{4+} does not have a significant effect on the permittivity of $Ba(CoTi)_xFe_{12-2x}O_{19}$@$BiFeO_3$, while it has a significant effect on the permeability.[46] The μ' firstly increases and then decreases with the increase of x. Notably, the highest μ' of $Ba(CoTi)_xFe_{12-2x}O_{19}$@$BiFeO_3$ is about 20.86 when $x = 1.2$, which is almost equal to ε'.

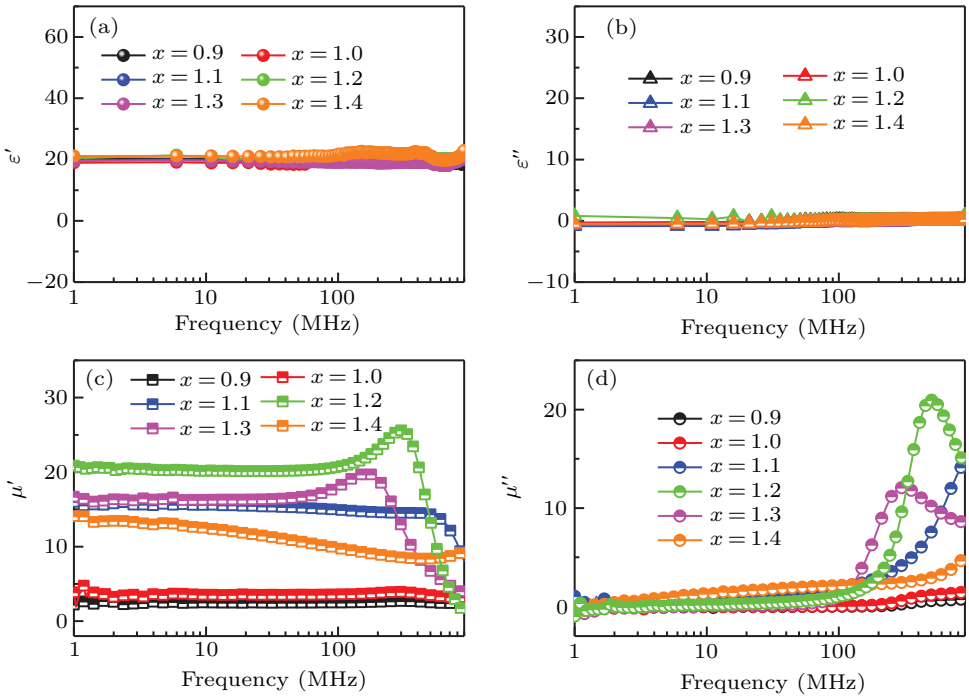


Fig. 4. (a) and (b) The complex permittivity of $Ba(CoTi)_xFe_{12-2x}O_{19}$@$BiFeO_3$ with various x, (c) and (d) the complex permeability of $Ba(CoTi)_xFe_{12-2x}O_{19}$@$BiFeO_3$ with various x.

The complex permeability of $Ba(CoTi)_xFe_{12-2x}O_{19}$@ $BiFeO_3$ mainly depends on two types of moment dynamics. One is the domain wall motion, and the other is the spin rotation. To further study the contribution of these two mechanisms to the complex permeability, the measured complex permeability spectrum is fitted by the domain wall motion and spin rotation mechanism

$$\mu' = 1 + \frac{\omega_d^2 \chi_d \left(\omega_d^2 - \omega^2\right)}{\left(\omega_d^2 - \omega^2\right)^2 + \omega^2 \beta^2} + \frac{\chi_s \omega_s^2 \left[\left(\omega_s^2 - \omega^2\right) + \omega^2 \alpha^2\right]}{\left[\omega_s^2 - \omega^2 (1+\alpha^2)\right]^2 + 4\omega^2 \omega_s^2 \alpha^2}, \tag{2}$$

$$\mu'' = \frac{\omega_d^2 \chi_d \omega \beta}{\left(\omega_d^2 - \omega^2\right)^2 + \omega^2 \beta^2} + \frac{\chi_s \omega_s^2 \omega \alpha \left[\omega_s^2 + \omega^2 \left(1+\alpha^2\right)\right]}{\left[\omega_s^2 - \omega^2 (1+\alpha^2)\right]^2 + 4\omega^2 \omega_s^2 \alpha^2}, \tag{3}$$

where χ_d is the static susceptibility provided by the domain wall motion mechanism, ω_d is the angular frequency of the domain wall resonance, β represents the damping factor of the domain wall motion mechanism, χ_s is the static susceptibility of the spin rotation mechanism, ω_s is the angular frequency of the natural resonance, α represents the damping factor of the spin rotation mechanism, and ω is the angular frequency of the applied magnetic field ($\omega = 2\pi f$).

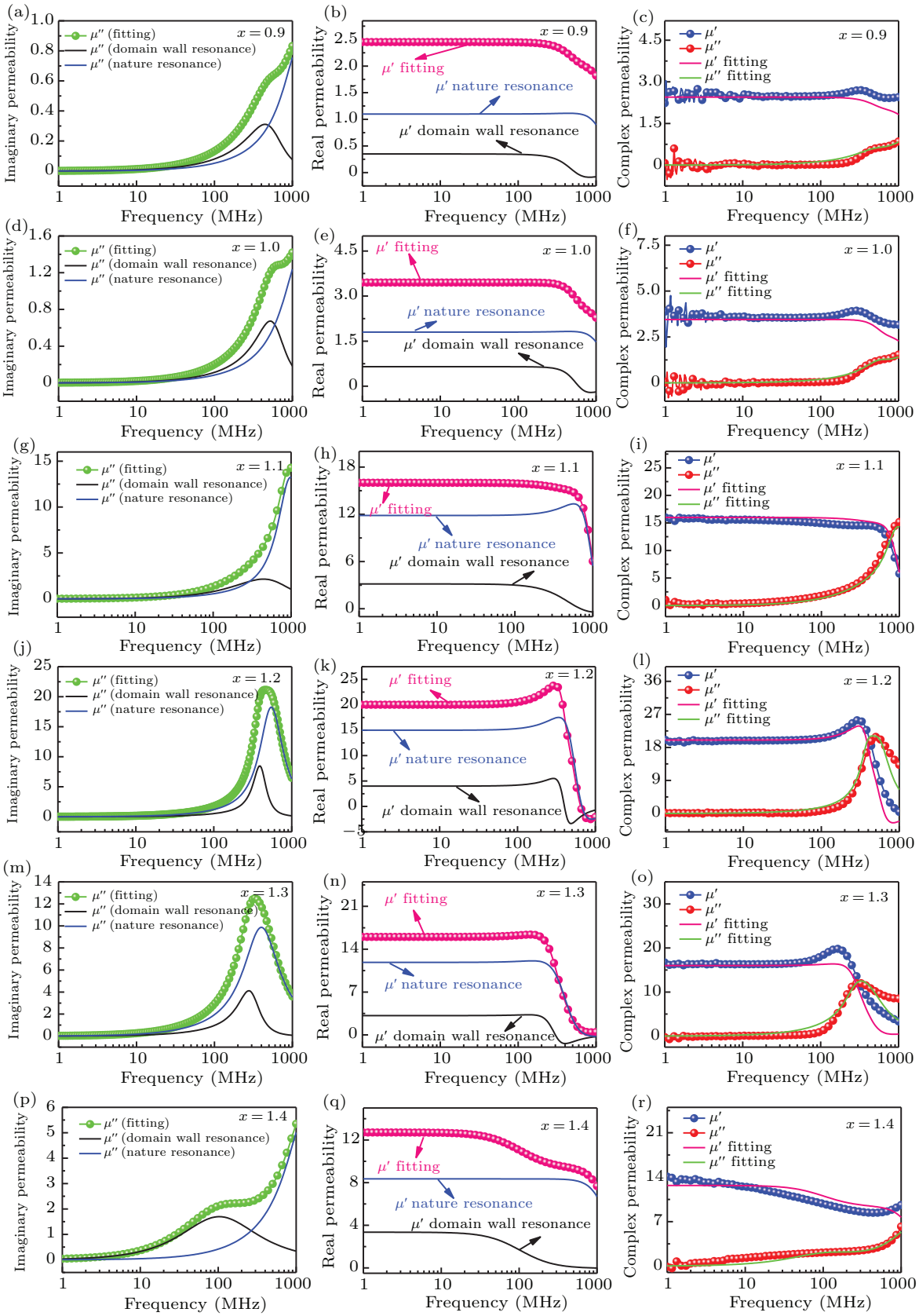


Fig. 5. Theoretical imaginary and real part of the permeability dispersion spectra, and the comparison of theoretical and measured complex permeability dispersion spectra; (a)–(c) $x = 0.9$, (d)–(f) $x = 1.0$, (g)–(i) $x = 1.1$, (j)–(l) $x = 1.2$, (m)–(o) $x = 1.3$, (p)–(r) $x = 1.4$.

Firstly, the above mentioned parameters can be obtained to simulate the measured imaginary part of the permeability spectrum by using Eq. (3). The simulation results are shown in Figs. 5(a), 5(d), 5(g), 5(j), 5(m), and 5(p). These parameters were then substituted into Eq. (2) to obtain the real part of the permeability spectrum, as shown in Figs. 5(b), 5(e), 5(h), 5(k), 5(n), and 5(q). The measured and simulated curves are shown in Figs. 5(c), 5(f), 5(i), 5(l), 5(o), and 5(r), respectively. The good overlap between the fitted and measured permeability amply proves that the magnetization process includes domain wall motion and spin rotation mechanisms. According to the fitted results, the spin rotation component significantly affects the permeability dispersion spectra compared to the domain wall movement component.

3.5. EM wave absorption properties

The EM wave absorption properties of $Ba(CoTi)_xFe_{12-2x}O_{19}$@$BiFeO_3$ can be characterized by its *RL*–*f* curves. Based on the transmission line theory, the *RL*–*f* curves with a certain thickness can be calculated from the complex permeability and permittivity by the following equation:[47]

$$Z = \frac{Z_{\text{in}}}{Z_0} = \sqrt{\frac{\mu_{\text{r}}}{\varepsilon_{\text{r}}}} \tanh\left(\text{j}\frac{2\pi f t}{c}\sqrt{\varepsilon_{\text{r}}\mu_{\text{r}}}\right), \tag{4}$$

$$RL\,(\text{dB}) = 20\text{Log}\left|\frac{Z-1}{Z+1}\right|, \tag{5}$$

where Z_{in} is the input impedance, Z_0 is the impedance in free space, μ_{r} and ε_{r} are the complex permeability and permittivity, respectively, f is the frequency of the EM wave, t is the thickness of the absorber, and c is the velocity of light in free space.

Figures 6(a)–6(f) show the thickness dependence of the *RL*–*f* curves for the $Ba(CoTi)_xFe_{12-2x}O_{19}$@$BiFeO_3$ with various x. As shown in Figs. 6(a) and 6(b), the samples with $x = 0.9$ and 1.0 display poor EM wave absorption properties with the minimum value of reflection loss (RL_{min}) above −10 dB when thickness is from 2.0 mm to 4.0 mm. As shown in Fig. 6(c), when x increases to 1.1, the RL_{min} reaches −34.43 dB at 955 MHz and the effective bandwidth is 120 MHz (880 MHz–1 GHz) for a thickness of 3.5 mm. The sample with $x = 1.2$ exhibits extremely good EM wave absorption properties, as shown in Fig. 6(d). Its RL_{min} can reach −30.42 dB at 617 MHz and the corresponding effective bandwidth reaches 563 MHz in the range of 437 MHz–1 GHz when the thickness is 3.5 mm. The sample with $x = 1.3$ also shows excellent EM wave absorption properties. Its RL_{min} reaches −40.63 dB at 910 MHz and the effective bandwidth is 190 MHz (810 MHz–1 GHz) for a thickness of 4 mm, as shown in Fig. 6(e). For the sample with $x = 1.4$, the EM wave absorption properties are slightly decreased. The RL_{min} reaches −25.41 dB at 990 MHz and the effective bandwidth is 22 MHz (978 MHz–1 GHz) for a thickness of 3 mm, as shown in Fig. 6(f).

It is well known that good impedance matching properties are the necessary condition for excellent EM wave absorption properties.[48,49] Figures 7(a)–7(f) show the relative input impedances ($|Z_{\text{in}}/Z_0|$) versus frequency of $Ba(CoTi)_xFe_{12-2x}O_{19}$@$BiFeO_3$ with a thickness of 2–4 mm. It can be clearly seen that the value of $|Z_{\text{in}}/Z_0|$ increases with frequency for samples with $x = 0.9$ and 1.0, but is much smaller than 1.0 in the megahertz band. Therefore, their EM wave absorption properties are poor due to the impedance mismatch and the low permeability. For samples with $x = 1.1$, 1.2, 1.3 and 1.4, the impedance matching properties are improved due to increased permeability, the $|Z_{\text{in}}/Z_0|$ value firstly increases and then decreases with frequency, and approach 1.0 at relatively high frequency bands (400 MHz–1 GHz), which means that these samples may obtain better microwave absorption properties in high frequency bands.

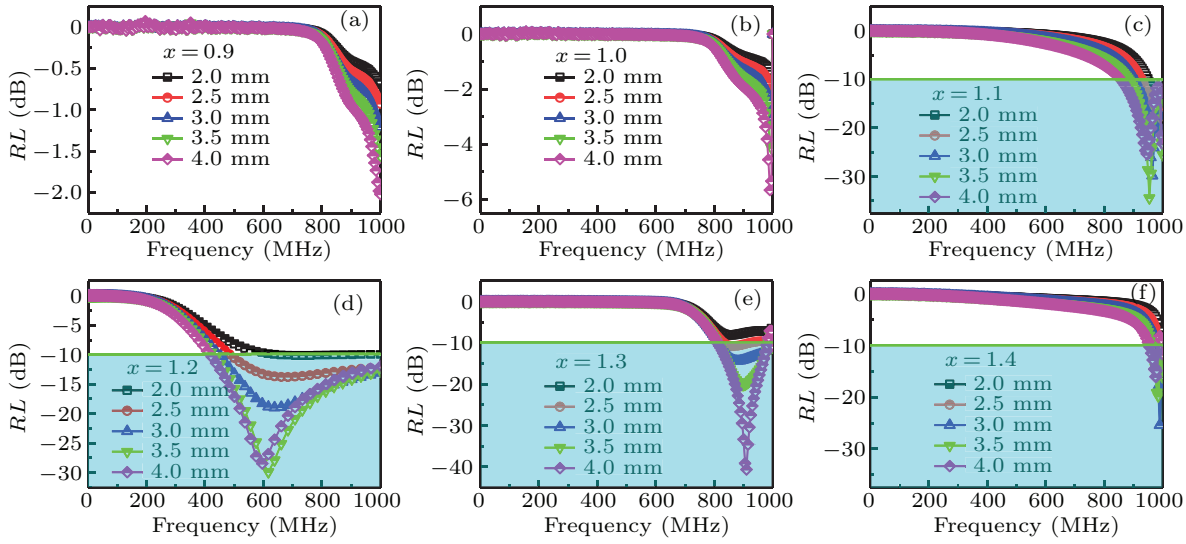


Fig. 6. Thickness-dependent *RL*–*f* curves of $Ba(CoTi)_xFe_{12-2x}O_{19}$@$BiFeO_3$ absorbers; (a) $x = 0.9$, (b) $x = 1.0$, (c) $x = 1.1$, (d) $x = 1.2$, (e) $x = 1.3$, and (f) $x = 1.4$.

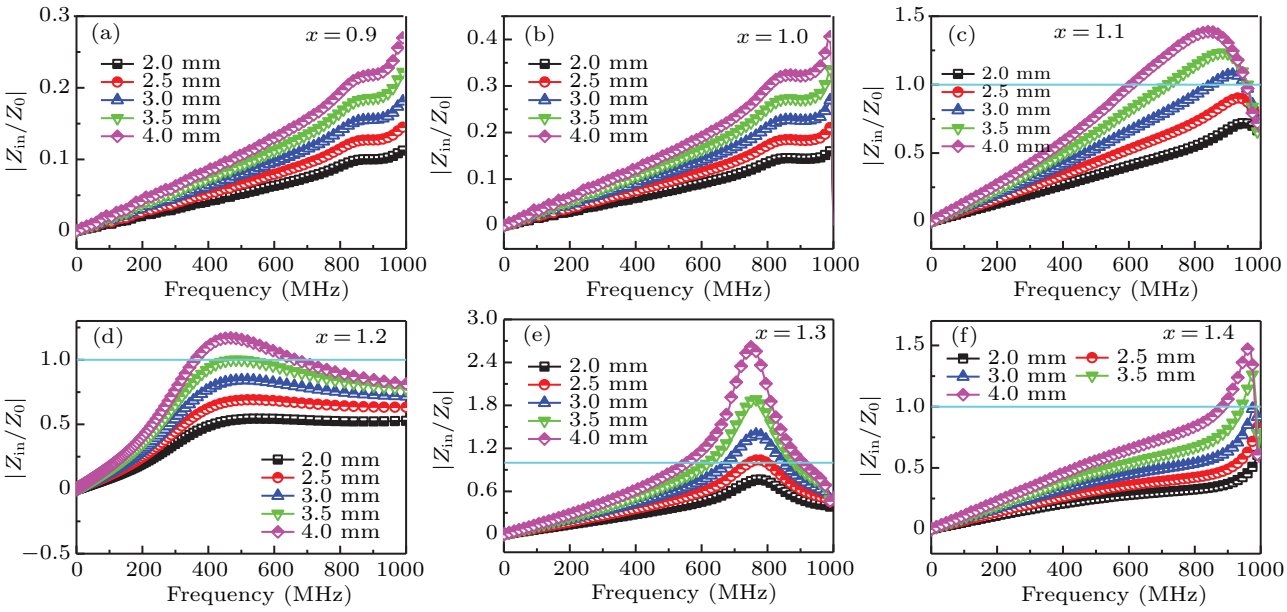


Fig. 7. The dependence of the relative input impedance $|Z_{in}/Z_0|$ on the frequency for $Ba(CoTi)_xFe_{12-2x}O_{19}$@$BiFeO_3$; (a) $x = 0.9$, (b) $x = 1.0$, (c) $x = 1.1$, (d) $x = 1.2$, (e) $x = 1.3$, (f) $x = 1.4$.

3.6. EM wave absorption mechanism

It can be seen from Fig. 6(d) that the *RL* peak frequency of the sample with $x = 1.2$ moves from 661 MHz to 596 MHz and the intensity firstly increases then decreases with the absorber thickness increases from 2.5 mm to 4.0 mm. This phenomenon can be explained by the interface cancelation model.[50,51] According to the interface cancelation model

$$t_m = \frac{(2k-1)c}{4f_m n}, \tag{6}$$

where t_m and f_m are matching thickness and matching frequency of a *RL* peak, ε_r and μ_r are complex permittivity and permeability, and c is the velocity of light, k is a positive integer, $n = \mathrm{Re}[\sqrt{\varepsilon_r \mu_r}]$,[52] the *RL* peak frequency is inversely proportional to the thickness of the absorber. Therefore, the *RL* peak moves to lower frequency with the increase of absorber thickness. In addition, the strong magnetic resonance shown in Fig. 4(d) can be found around 600 MHz. The loss inside the absorber may also play an important role in the absorption of EM waves for $Ba(CoTi)_{1.2}Fe_{9.6}O_{19}$@$BiFeO_3$.[34,35]

In our previous study, a symmetry model was proposed to separate the internal loss and the interface cancelation.[53] The reflected waves originating from the front (W_1) and back (W_2) interfaces of absorber were separated by using the symmetry model to calculate the internal energy loss (E_{loss}) and interface cancelation energy loss (E'_{loss}) of $Ba(CoTi)_xFe_{12-2x}O_{19}$@$BiFeO_3$ absorber with $x = 1.2$. Assuming that the energy of incident EM wave is 1, then the total energy (E_{total}) absorption by the absorber can be calculated by its *RL*–*f* curves

$$E_{total} = 1 - 10^{\frac{RL}{10}}, \tag{7}$$

the total energy absorption by the absorber includes the part of interface cancelation and the part of internal loss

$$E_{total} = E'_{loss} + E_{loss}, \tag{8}$$

among them, the energy of the EM wave loss inside (E_{loss}) the absorber can be calculated by separating waves W_1 and W_2

$$E_{loss} = 1 - 10^{\frac{W_1}{10}} - 10^{\frac{W_2}{10}}, \tag{9}$$

the calculation results are shown in Figs. 8(a)–8(d), where the blue solid lines represent the total energy (E_{total}) absorbed by the absorbers, the red solid lines represent the attenuated energy (E_{loss}) of the EM waves inside the absorber, and the solid green lines represent the cancelation energy (E'_{loss}) of reflected waves at the front and back interfaces, and the symbol lines represent the *RL*–*f* curves. It can be seen that the red solid lines are much higher than the green solid lines in the effective absorption frequency band ($RL \leq -10$ dB). This means that the absorption of EM waves by the absorber mainly originates from the high loss inside the absorber. The internal loss mainly comes from the magnetic loss caused by the natural resonance.[54] As shown in Fig. 8(a), when the thickness of the absorber is 2.5 mm, E_{loss} accounts for 56%–77% of the incident wave energy, the bandwidth is 514 MHz. The E_{loss} increases with the increasing thickness of the absorber. When the thickness of the absorber reaches 4 mm, E_{loss} accounts for 63%–85% of the incident wave energy, and the bandwidth reaches 585 MHz. This indicates that high internal loss can increase the bandwidth of the absorber.

For absorber with a thickness of 3.5 mm, E_{loss} increases with frequency, and the maximum value at 1 GHz is about 83% (−7.70 dB) of the energy of the incident wave, which does not

match with the frequency and intensity of the *RL* peak. It indicates that strong absorption peaks cannot be achieved by only internal loss. $E'_{\rm loss}$ firstly increases and then decreases with frequency, the maximum value of $E'_{\rm loss}$ moves to lower frequency with the increase of absorber thickness. The *RL*–*f* curves exhibit the same trend with the variation of frequency and thickness. This further indicates that the *RL* peaks are attributed to interface cancelation. The interface cancelation enhances the absorption properties and generates sharp absorption peaks (−30.42 dB). From above discussions, it can be concluded that the excellent wave absorption properties are based on the combination of high loss inside the absorber and the interface cancelation. The frequency and intensity of *RL* peak are mainly determined by the interface cancelation, and the internal loss plays a crucial role in expanding the bandwidth.

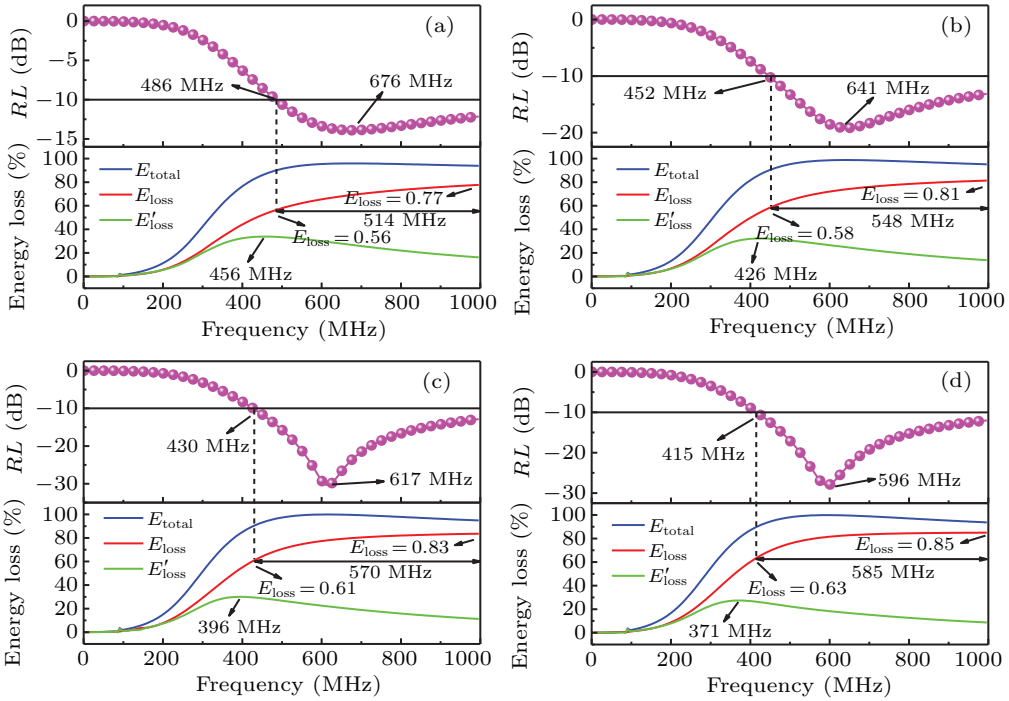


Fig. 8. The total energy loss (blue lines), internal energy loss (red lines), interface cancelation energy loss (green lines) and *RL*–*f* curves (symbol lines) of the absorber with various thickness (a) 2.5 mm, (b) 3.0 mm, (c) 3.5 mm, (d) 4.0 mm.

4. Conclusion

Herein, the $Ba(CoTi)_xFe_{12-2x}O_{19}$@$BiFeO_3$ EM wave absorption material with different Co^{2+}−Ti^{4+} content is successfully prepared, and its low−frequency EM wave absorption properties are investigated. The experimental results show that $Ba(CoTi)_xFe_{12-2x}O_{19}$@$BiFeO_3$ exhibits excellent wave absorption properties at different Co^{2+}–Ti^{4+} content. The best comprehensive property is obtained for $x = 1.2$, in which case, the absorber has the highest permeability, internal loss and the best impedance matching properties, where the $RL_{\rm min}$ and effective bandwidth are −30.43 dB, 617 MHz, respectively. The investigation on absorption mechanism shows that the strong EM wave absorption properties of $Ba(CoTi)_xFe_{12-2x}O_{19}$@$BiFeO_3$ are mainly originated from the internal loss caused by natural resonance, and the interface cancelation of the reflected waves from the front and back interfaces further improves the absorption intensity and generates a *RL* peak.

Acknowledgements

Project supported by the National Natural Science Foundation of China (Grant No. 11574122) and the Joint Fund of Equipment Pre-Research and Ministry of Education, China (Grant No. 6141A02033242).

References

[1] Liu J, Zhang L and Wu H 2021 *J. Phys. D* **54** 203001
[2] Solgi S, Seyed Dorraji M S, Hosseini S F, Rasoulifard M H, Hajimiri I and Amani-Ghadim A 2021 *Sci. Rep.* **11** 19339
[3] Zeng X, Cheng X, Yu R and Stucky G D 2020 *Carbon* **168** 606
[4] Gao S, Wang G S, Guo L and Yu S H 2020 *Small* **16** 1906668
[5] Xiao L X, Jin Z, Xia Z C, Shi L R, Huang J W, Chen B R, Shang C, Wei M and Long Z 2015 *Chin. Phys. Lett.* **32** 017501
[6] Zhao K H, Wang Y H, Shi X L, Liu N and Zhang L W 2015 *Chin. Phys. Lett.* **32** 027501
[7] Zhao K H, Wang Y H, Shi X L, Liu N and Zhang L W 2015 *Chin. Phys. Lett.* **32** 087503
[8] Li X Y, Zhao L, Wei X Y, Li H and Jin K X 2018 *Chin. Phys. B* **27** 117501
[9] Sun X D, Xu B, Wu H Y, Cao F Z, Zhao J J and Lu Y 2017 *Acta Phys. Sin.* **66** 157501 (in Chinese)
[10] Gong B C, Yang H C, Jin K, Liu K and Lu Z Y 2020 *Chin. Phys. B* **29** 077508

[11] Cui Q, Cai Y Q, X Li, Dun Z L, Sun P J, Zhou J S, Zhou H D and Cheng J G 2020 *Chin. Phys. B* **29** 047502
[12] Li Y W, Song J, Wei J L, Zhou Y B and Li G 2014 *Appl. Mech. Mater.* **577** 48
[13] Xue W, Yang G, Bi S, Zhang J and Hou Z L 2021 *Carbon* **173** 521
[14] Wu C, Maier J and Yu Y 2016 *Adv. Mater.* **28** 174
[15] Wang Y, Du Y, Xu P, Qiang R and Han X 2017 *Polymers (Basel)* **9** 29
[16] Wu Y P, Ong C K, Lin G Q and Li Z W 2006 *J. Phys. D: Appl. Phys.* **39** 2915
[17] Peng L, Hu Y B, Guo C, Li L Z, Wang R, Hu Y and Tu X Q 2015 *Chin. Phys. Lett.* **32** 017502
[18] Wang Z L, Ma H, Wang F, Li M, Zhang L G and Xu X H 2016 *Chin. Phys. Lett.* **33** 107501
[19] Liu D, Gao S, Jin R, Wang F, Chu X, Gao T and Wang Y 2019 *Chin. Phys. B* **28** 057503
[20] Cheng Y, Ji G, Li Z, Lv H, Liu W, Zhao Y, Cao J and Du Y 2017 *J. Alloys Compd.* **704** 289
[21] Zheng J, Du K, Xiao D, Zhou Z Y, Wei W G, Chen J J, Yin L F and J Shen 2016 *Chin. Phys. Lett.* **33** 097501
[22] He X M, Zhong W and Du Y W 2018 *Acta Phys. Sin.* **67** 227501 (in Chinese)
[23] Hu Q, Qiao G, Yang W, Liu Z, Zhang P, Liu S, Wang C, Zhou D, Han R, Cai D, Hu B and Yang J 2020 *J. Phys. D* **53** 115001
[24] Sheng J M, Kan X C, Ge H, Yuan P Q, Zhang L, Zhao N, Song Z M, Yao Y Y, Tang J N, Wang S M, Tian M L, Tong X and Wu L S 2020 *Chin. Phys. B* **29** 057503
[25] Wang W, Guo J, Long C, Li W and Guan J 2015 *J. Alloys Compd.* **637** 106
[26] Wang X, Song K, Gong W, Luo H, Yan S and Gong R 2016 *IEEE Trans. Magn.* **52** 1
[27] Sugimoto S, Haga K, Kagotani T and Inomata K 2005 *J. Magn. Magn. Mater.* **290–291** 1188
[28] Li D M, Fang S K, Tong J S, Su J, Zhang N and Song J L 2018 *Acta Phys. Sin.* **67** 067501 (in Chinese)
[29] Wang F, Long C, Wu T, Li W, Chen Z, Xia F, Wu J and Guan J 2020 *J. Alloys Compd.* **823** 153827
[30] Shu J C, Huang X Y and Cao M S 2021 *Carbon* **174** 638
[31] Peng H, Ma X, Liu C, Lei C, Li X and Xiong Z 2021 *J. Alloys Compd.* **889** 161636
[32] Houbi A, Aldashevich Z A, Atassi Y, Bagasharova Telmanovna Z, Saule M and Kubanych K 2021 *J. Magn. Magn. Mater.* **529** 167839
[33] Li J, Xu T, Liu L, Hong Y, Song Z, Bai H and Zhou Z 2021 *Ceram. Int.* **47** 19247
[34] Chang Y, Zhang Y, Meng C, Liu S, Chang H and Liu Z 2020 *Appl. Phys. Lett.* **116** 082404
[35] Sözeri H, Deligöz H, Kavas H and Baykal A 2014 *Ceram. Int.* **40** 8645
[36] Gan G, Zhang H, Li Q, Li J, Li M, Xu F and Jing Y 2018 *Mater. Res. Bull.* **97** 37
[37] Yang Y, Zhang H, Li J, Rao Y, Wang G and Gan G 2020 *Ceram. Int.* **46** 25697
[38] Gan G, Zhang D, Li J, Wang G, Huang X, Yang Y, Rao Y, Wang X and Zhang H 2020 *Ceram. Int.* **46** 27996
[39] Gan G, Zhang D, Li J, Wang G, Huang X, Rao Y, Yang Y, Wang X, Zhang H, Chen R T 2020 *Ceram. Int.* **46** 8398
[40] Wang X, Yin K, Cao T, Liao Y, Wang Z, Kou Q and Cheng D 2021 *J. Alloys Compd.* **885** 160983
[41] Xu J, Lin P, Chen Q, Zhao X, He P, Lin T, Jiang C, Liu Y, Liu H and Long W 2021 *Ceram. Int.* **47** 973
[42] Tehrani M K, Ghasemi A, Moradi M and Alam R S 2011 *J. Alloys Compd.* **509** 8398
[43] Chawla S K, Mudsainiyan R K, Meena S S and Yusuf S M 2014 *J. Magn. Magn. Mater.* **350** 23
[44] Morrish A H, Zhou X Z, Yang Z and Zeng H X 1994 *Hyperfine Interact.* **90** 365
[45] Li J, Zhang H, Liu Y, Liao Y, Ma G and Yang H 2015 *Mater. Res. Express* **2** 046104
[46] Wang C, Li L T, Zhou J, Qi X W and Yue Z X 2002 *J. Mater. Sci.* **13** 713
[47] Ma G, Duan Y, Liu Y and Gao S 2018 *J. Mater. Sci.* **29** 17405
[48] Ge C, Wang L, Liu G and Wang T 2018 *J. Alloys Compd.* **767** 173
[49] Yan L, Wang J, Han X, Ren Y, Liu Q and Li F 2010 *Nanotechnology* **21** 095708
[50] Wang T, Wang H, Tan G G, Wang L and Qiao L 2015 *IEEE Trans. Magn.* **51** 1
[51] Wang T, Han R, Tan G, Wei J, Qiao L and Li F 2012 *J. Appl. Phys.* **112** 104903
[52] Tang M, Zhang J Y, Bi S, Hou Z L, Shao X H, Zhan K T and Cao M S 2019 *ACS Appl. Mater. Inter.* **11** 33285
[53] Zhang J, Wang P, Wang G, Duan B, Wang T and Li F 2020 *J. Magn. Magn. Mater.* **498** 166096
[54] Dong C, Wang X, Zhou P, Liu T, Xie J and Deng L 2014 *J. Magn. Magn. Mater.* **354** 340